Hysteresis in Relative Permeability from Cyclic Water-Oil Corefloods

Victor Fernandes[1,*], *Halidi* Abdoulghafour[1,2], *Amin* Rezaei[1,2], *Fabrice* Pairoys[3], *Marcel* Bourgeois[1], *Franck* NONO[1] and *Cyril* Caubit[1]

[1]TotalEnergies, CSTJF, Avenue Larribau, 64000 Pau, France
[2]Akkodis, 64000 Pau, France
[3]SLB, Doha, Qatar

Abstract. Water injection is a long-standing method for secondary oil recovery, benefiting from favorable water/oil mobility. However, ultimate recovery can be limited by gravity segregation in thick reservoirs, snap-off trapping in water-wet rocks, and low mobility in viscous oil systems. This study investigates relative permeability hysteresis through six cyclic coreflooding experiments WOWO (Water-Oil-Water-Oil) on turbidite sandstones with diverse porosity and permeability. The goal is to derive drainage and imbibition Kr curves under high interfacial tension conditions, evaluating hysteresis and saturation path effects. Water/oil tests used formation brine and dead oil at reservoir temperature and 10 bar pore pressure. 2D X-ray imaging enabled visualization of fluid fronts and capillary end-effects. Results revealed phase-dependent hysteresis, as WOWO tests exhibited cycle-dependent hysteresis, leading to fluid trapping, mobility reduction, and deviations in Kr and Pc behavior from conventional simulator models.

1 Introduction

Two-phase relative permeability curves exhibit pronounced hysteresis because the pore-scale configuration of fluids during coreflood (layers, films, ganglia) depend on the flow history. Relative permeability hysteresis arises from contact-angle hysteresis and capillary trapping of the nonwetting phase [1], which impacts fluid flow at the pore scale. During imbibition in water-wet systems, water tends to spread along grain surfaces, and oil snap-off in constrictions occurs, isolating oil droplets or layers [2]. These trapped oil ganglia become immobile, creating a residual oil saturation that depends on how the pore network was flooded [3]. In fact, strong hysteresis was observed in the relation between disconnected (trapped) oil saturation and overall water saturation in water-wet media [1]. By definition, considering a water-wet rock that was waterflooded at capillary-dominated regime (Ca below 10E-06), residual oil is the volume of oil partitioned into isolated ganglia surrounded by water, and thus unavailable to flow.

In a typical water-wet waterflood, snap-off and cooperative pore-filling control how much oil gets trapped when water advances, whereas on oil invasion during drainage, oil tends to flow piston-like through the network of pores connected by large throats. As a result, the water (wetting) relative permeability curve typically shows little to no change between flow cycles, whereas the oil (nonwetting) curve drops significantly due to trapping that leads to mobility reduction. Under cyclic drainage–imbibition, the nonwetting-phase relative permeability exhibits strong hysteresis driven by corner-filling (snap-off) mechanisms, while the wetting-phase curves remain nearly reversible [1].

Wettability and pore-structure history play a key role in relative permeability hysteresis and oil recovery. In strongly water-wet systems, oil is displaced primarily by piston-like imbibition, with snap-off events leading to disconnected oil ganglia and often high residual oil saturations. In contrast, strongly oil-wet media allow water to invade preferentially through larger pores, bypassing oil that remains as continuous films along pore walls. Although this behavior initially results in low recovery during waterflooding, several studies have shown that oil-wet systems may continue to slowly recover oil due to film and layer drainage, indicating that ultimate recovery may be higher than early-time results suggested [4]. Jadhunandan and Morrow found that maximum recovery typically occurs in intermediate-wet systems, where both oil and water phases exhibit favorable mobility and trapping is minimized [5].

The path of saturation change is equally important. When flow is reversed or cycled, the system follows scanning curves between the primary drainage and imbibition limits. Each reversal resets the effective residual saturation based on how much oil was trapped during the previous phase. Thus, in cyclic imbibition–drainage–imbibition-drainage (WOWO) flooding, the history of saturation – including the number of pore volumes injected and the sequence of water and oil injection – determines the current state and the subsequent flow behavior. Traditional hysteresis models, including those proposed by Land [11], Carlson [12], and Killough [6], have provided valuable insights for decades but remain limited in their applicability to mixed-wet systems and different cyclic flow scenarios. These models are thoroughly reviewed and critiqued in Spiteri et al. [4], especially in the sections

---

* Corresponding author: victor.de-oliveira-fernandes@totalenergies.com*

discussing limitations of the Land and Carlson approaches in predicting behavior in intermediate- and oil-wet systems.

Killough's model builds on Land's trapping concept and computes scanning relative-permeability curves by interpolation or normalization from the main curves [6]. Importantly, Killough assumed no additional trapping of the wetting phase on reversal, so that the wetting-phase curves do not exhibit hysteresis, while all trapping effects occur for the nonwetting phase during imbibition.

Traditional models frequently use fixed boundary curves and assume straightforward changes in fluid saturation. However, they often fall short in accurately representing the complex behaviors seen in mixed-wet or oil-wet reservoirs. For instance, in these environments, increasing the initial amount of oil doesn't always lead to more residual oil after water flooding - a non-linear relationship that standard models are unable to capture. Additionally, the paths that describe how easily fluids flow during scanning curves can have intricate shapes in such reservoirs, which these models fail to represent accurately. The Land model is limited to water-wet conditions and lacks flexibility, as it considers monotonic behavior of initial/trapped oil saturation. Killough's approach, though implemented in many simulators, assumes full reversibility in imbibition and does not account for wetting-phase hysteresis. Carlson's model includes a geometric trapping mechanism but similarly ignores wetting-phase hysteresis, limiting its applicability on wetting states other than water-wet. More recent models—like Beattie's [7], which introduces flexibility via normalization, and Kjosavik's [8], which adapts Land's trapping for mixed-wet systems, offer broader applicability but require careful parameter selection and still rely on empirical assumptions. Recent advances have sought to address these gaps. Spiteri et al. [9] introduced a wettability-sensitive trapping and relative permeability model capable of capturing curve crossings and non-monotonic saturation trends across a range of wettability states. Similarly, generalized capillary pressure correlations have been developed to bridge primary drainage, imbibition, and scanning loops in mixed-wet media, offering a more continuous description of multiphase flow behavior. One such model is proposed in Skjaeveland et al. [10]. Yet, experimental datasets for validating such models, particularly under controlled multiphase flow conditions with cyclic injection, remain scarce.

This study aims to fill that gap by presenting a detailed experimental investigation into relative permeability hysteresis during cyclic water/oil coreflooding. A total of six WOWO experiments were conducted on turbidite sandstones with wide-ranging petrophysical properties. The tests were designed to generate both drainage and imbibition flow paths, under conditions representative of field-scale EOR operations. Coreflood experiments were conducted at temperatures close to that of the reservoir (90 °C for the coreflood and 125 °C in the reservoir) and 10 bar pore pressure using formation brine and dead oil. Throughout the experiments, fluid behavior was continuously monitored via 2D X-ray imaging, enabling visualization of front dynamics and accurate quantification of capillary end-effects. These methods build directly on experimental SCAL practices used in literature, and integrate imaging techniques for capturing end effects similar to those mentioned in Egermann et al. [11].

Beyond characterizing relative permeability hysteresis, these experiments are designed to emulate key aspects of multiphase flow behavior observed in EOR processes. WOWO coreflood tests replicate alternating fluid invasion sequences that commonly occur near the water/oil contact (WOC) during secondary or tertiary water injection. In such field scenarios, displacement cycles arise as injection wells are placed near or below the WOC, causing the saturation front to alternate between imbibition and drainage. Laboratory WOWO protocols mimic these dynamics under controlled conditions, offering critical insight into saturation-path–dependent hysteresis, wettability evolution, and capillary trapping. Repeated cycling allows for systematic observation of how residual oil saturation and relative permeability evolve over time, particularly in mixed- and oil-wet systems. Finally, the hysteresis behavior from our WOWO tests is interpreted using the Killough model: because Killough's formulation effectively captures the history-dependent wetting-phase curves for oil–water systems [12], it provides a suitable framework for our predominantly mixed- and oil-wet core data. In the sections that follow we present the WOWO experiments and discuss the implied pore-scale mechanisms, showing how wettability and saturation path control the observed hysteresis.

2 Methodology

2.1 Core and fluid preparation

Cylindrical core samples of 50 mm in diameter and 200 mm in length used for the W/O cyclic injection tests were extracted from different turbidite reservoirs in two South American fields. Each core is labeled with a code that incorporates three key elements: the first letter indicates the field of origin, the following characters (i.e., LT1, LT2, LT3) designate the core name, and the final number represents the sedimentary classification. This classification is derived from geological descriptions of the core material, with details provided in Table 1.

Table 1. Sedimentary classification description

Sedimentary classification	Description
8	Massive fine to medium high density turbiditic sand
9	Laminated fine to medium sand
10	Massive coarse to gravelly high density turbiditic sand

Prior to the coreflood experiments, the cores were imaged by computed tomography to assess general homogeneity and core overall integrity. A CT scan image of each core is presented in the Appendix section. Cores present overall homogeneity with varied grain sizing and sorting. In addition, no fractures or visible fissures are observed. Cores KLT2-8 and KLT2-9 present laminations transversal to fluid flow, that does not impact multiphase flow, as they are perpendicular to flow.

The preserved samples were then cleaned using solvent flushing until clear effluents were observed, followed by saturation with toluene to enable miscible displacement with heptane. This operation is called miscible tracer test and consists in the miscible replacement of a resident phase by another one having approximately the same viscosity but different density. Density evolution is measured downstream the core and allows the characterization of the dispersive behaviour of the sample and potential longitudinal heterogeneities. The shape of the injected fluid concentration as a function of its injected volume is a diagnosis of heterogeneity. The following indicators are used to provide an assessment of the core longitudinal homogeneity:

i) Peclet Number (Pe) >> 1: the test must be carried out at high Peclet Number to put in evidence of heterogeneity. The Peclet Number is defined by eq (1):

$$Pe = \frac{u * d_p}{D_d} \tag{1}$$

where u is the Darcy velocity, d_p is the characteristic pore length and D_d is the coefficient of molecular diffusion.

ii) Injected fluid breakthrough (BT) after 0.6 pore volumes (PV) injected.

iii) Normalized concentration lower than 0.6 at 1 PV injected.

iv) Normalized concentration stabilization before 1.5 PV.

The miscible tracer tests curves are presented in the Appendix.

Routine core characterization, including porosity and absolute permeability measurements using both gas and formation brine, was conducted on all samples. Porosity and permeability measurements performed using different methods on these samples aim to assess the consistency and repeatability of the results, both in terms of pore volume and rock permeability.

The corresponding core samples sedimentary classification, effective porosity, absolute (liquid) permeability and dispersion coefficients (Peclet Number) are summarized in Table 2.

Table 2. Core samples identification, sedimentary classification, effective porosity, water permeability and Peclet Number during miscible tracer test

Cores	PhiE (frac.)	Kw (mD)	Pe (dimension-less)
SLT1-10	0.190 ± 0.007	3060 ± 25	80
SLT2-10	0.201 ± 0.007	2198 ± 19	213
KLT2-8	0.288 ± 0.007	170 ± 3	170
KLT1-8	0.180 ± 0.007	530 ± 4	119
KLT2-9	0.227 ± 0.007	157 ± 1	340
KLT3-10	0.133 ± 0.007	80 ± 1	144

The water-oil experiments were performed in immiscible conditions using synthetic brine following formation brine composition and dead oil extracted from the corresponding reservoir/well. Oil-water interfacial tension (IFT) is measured to attest that the dead oil is not contaminated with demulsifiers that could impact wettability restoration. IFT tests are performed at room temperature and using distilled water and the results range between 24 dyn/cm and 28 dyn/cm.

The formation brines used in the experiments had NaCl-equivalent salinities 12.7 g/l for SLT samples and 18.9 g/l for KLT core samples.

To ensure representativity, the viscosity ratio between oil and brine under light conditions (90 °C and 10 bar pore pressure) was compared to that at reservoir conditions.

Typically, twin plugs (similar petrophysical properties and sedimentary classification) are selected at close depth to that of the tested core to characterize pore throat size distribution with MICP. The result of the selected MICP plugs referent to S and K fields are presented in the Appendix section.

2.2 Cores preparation for cyclic injection

2.2.1 Initial states restoration

The initial water saturation (Swi) is established by displacing brine from fully saturated cores via unsteady-state oil flooding using synthetic mineral oil. Prior to this, the cores were vacuum-saturated with brine, after which porosity and brine permeability were measured.

Primary drainage was performed by injecting mineral oil into the core at constant flow rate steps to reduce water saturation to the target Swi. The target Swi is defined by the water saturation associated with the depth at which the core was drilled in the reservoir. Therefore, target Swi may occasionally be higher than irreducible water saturation (Swirr). During this process, pressure drop across the core and water production were continuously monitored. Fluid saturation during oil injection was also tracked using the CXBOX—an in-situ saturation monitoring (ISSM) system that enables dopant-free, 2D saturation visualization via X-ray radiography [13]. This imaging device allows the acquisition of images of 200 µm resolution at every second, thus enabling thorough saturation path evolution. The quality of the ISSM data was validated by ensuring a deviation of less than 3% relative to material balance calculations.

Oils used for setting Swi depended on the rocks permeability: MarcolTM 82 (M82) was used for cores with permeability greater than 0.5 D, while MarcolTM 52 (M52) was selected for lower-permeability samples (<0.5 D). After setting Swi, the mineral oil is miscibly replaced by toluene in order to prevent direct contact between the mineral oil and dead oil, which could result in asphaltene precipitation. During this operation, Marcol is initially displaced by toluene, followed by the miscible displacement of toluene by dead oil at 60 °C. The 60 °C is chosen for keeping the core at least 15 °C above the wax appearance temperature (WAT), which could generate plugging. Temperature is then set to 90 °C and before-ageing dead oil permeability at Swi is measured. Wettability restoration is carried out for four weeks, with a flow direction reversal halfway through the cycle to prevent heterogeneous wettability generation [14]. Permeability measurements are performed after flow reversal and after ageing to monitor its evolution. After the four-weeks ageing step, the core states are considered restored, and the rock is ready to undergo the cyclic water/oil coreflood experiments.

Oil permeability at Swi measured before and after ageing are presented in Table 3.

Table 3. Before and after ageing dead oil permeability at Swi

Cores	$Ko(Swi)_{BA}$ (mD)	$Ko(Swi)_{AA}$ (mD)
SLT1-10	3535 ± 213	2990 ± 176
SLT2-10	2350 ± 140	2233 ± 137

KLT2-8	224 ± 21	222 ± 20
KLT1-8	500 ± 39	482 ± 39
KLT2-9	147 ± 7	136 ± 7
KLT3-10	75 ± 6	75 ± 6

2.2.2 Cyclic water/oil (WOWO) experiments

Cyclic water/oil unsteady-state coreflood experiments were conducted at 90 °C, close to reservoir conditions, under a constant pore pressure of 10 bar. Fluid saturation was continuously monitored throughout the coreflooding protocol using the CXBOX in-situ saturation monitoring system.

To ensure capillary-dominated flow and avoid viscous desaturation that could result in underestimation of residual saturations (ROS, RWS), the capillary number for all the flowrate steps was kept below $Ca \leq 10^{-5}$ [15]. The capillary number is defined by eq (2):

$$Ca = \frac{\mu * v}{\sigma} \tag{2}$$

where, μ is injected fluid viscosity, v is Darcy velocity and σ is the interfacial tension.

Additionally, the initial flow rate step for each test was selected to reproduce typical field velocities (1–2 feet/day), ensuring representative displacement conditions [16]. For the final flow steps, the Rapoport–Leas number (RL, expressed in $cm^2/min.cp$) exceeded 1.0, corresponding to the critical threshold for minimized end-effects [15].

One important clarification: synthetic mineral oil was used for the cyclic corefloods of core SLT2-10 due to a pressure buildup observed during the dynamic ageing phase at very low oil flow rates. To prevent plugging during coreflooding, the dead oil was replaced with synthetic isoparaffinic oil, and all injections were carried out from bottom to top at room temperature. This procedure was applied exclusively to core SLT2-10.

The WOWO experiment comprised four key phases: two forced imbibition cycles (Imbibition 1 and Imbibition 2) and two forced drainage cycles (Drainage 2 and Drainage 3). Drainage 1 corresponds to the primary drainage step, initial oil injection used to establish initial water saturation. The coreflooding sequence is illustrated in Fig. 1.

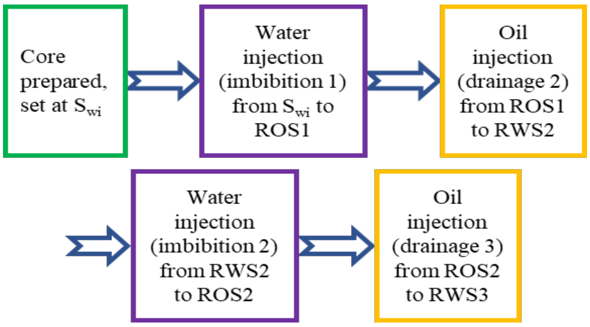

Fig. 1. Schematic representation of the WOWO experiment sequence.

During imbibition cycles, water is injected in stepwise manner increasing flow rates until oil production ceases, and the pressure drop (ΔP) across the core is stabilized. The final flow rate at which stabilization occurred defines the remaining oil saturation (ROS). Following this, water permeability at ROS was measured at multiple flow rates to determine the Krw endpoint for the relative permeability curve (Krw@ROS). This endpoint represents an experimental value associated to the ROS, as the residual oil saturation (S_{or}) and final Krw endpoint (Krw@S_{or}) are obtained after numerical simulation. 2D fluid saturation monitoring was performed throughout the experiment, which allowed us to assess the capillary end effects, that were present despite the bump rate performed. The presence of the capillary end effects is an important indicator that the measured values of Krw@ROS does not represent the actual Krw endpoint (Krw@ S_{or}).

Subsequently, drainage cycles involved injecting oil at increasing flow rates. After each stage of stabilized water production and ΔP, oil permeability was measured at the remaining water saturation (RWS), representing trapped water, to determine the Kro endpoint (the same comment regarding numerical interpretation for Krw endpoints applies to Kro).

The experimental data measured during the tests are history-matched through numerical simulation, that provides imbibition and drainage Kr and Pc curves. In this work, we used CYDAR® numerical simulator [17] for performing the history-match of the multiphase flow experiments. CYDAR® is a 1D numerical simulator for design and interpretation of SCAL experiments.

The boundary conditions for the numerical simulations of unsteady-state experiments are fully-described in [18].

There are numerous (and non-unique) solutions for the equations in coreflooding simulation. It is therefore essential to set as many input parameters as possible. For the imbibition and drainage cycles, the monitored data were as follows:

- Produced fluid volume (cc): oil during imbibition, water during drainage,
- Pressure drop (ΔP) between core end-faces,
- Longitudinal fluid saturation profiles (oil or water),
- Average fluid saturation is determined through material balance and in situ saturation monitoring (ISSM).

During the Kr and Pc interpretation process via history matching, we use the produced fluid volumes, and the pressure drop as objective functions during the optimization process. Saturation profiles are also used as objective functions, but with less weight on the optimization calculation. In addition, saturation profiles provide important insights to constrain Kr and Pc interpretation, that are:

i) Saturation value at core outlet provides a good estimation of the saturation at Pc= 0. We can establish a confidence interval around the observed saturation at the outlet (particularly important in the calculation of the Amott* values).

ii) Saturation value at core inlet provides good estimation of residual saturations (residual oil saturation – Sor – and irreducible water saturation -Swirr).

iii) Presence of capillary end-effects after bump rates indicate wettability to the resident fluid over the injected fluid (oil-wetness in case of imbibition processes, water-wetness in case of drainage processes).

Relative permeability and capillary pressure curves uncertainty estimation is a trending subject. Kr and Pc are obtained through a transient inverse analysis and there are numerous (and non-unique) solutions for the equations in coreflooding simulation. Therefore, Kr and Pc uncertainty is sensitive not only to measurement equipment uncertainty but also to the quality of the history match. That is why it is essential to define as many input parameters as possible to constrain the numerical simulation and reduce the solutions dimension. In the results and discussion section, the good quality history match of the extensive coreflood experimental dataset gives enough confidence to elaborate the conclusions presented in the end of the paper.

The CXBOX provides 2D saturation profiles monitoring, that are converted into 1D saturation profiles for the sake of the history match with CYDAR (1D numerical simulator).

A schematic of the experimental setup used for coreflooding experiments is illustrated in Fig. 2.

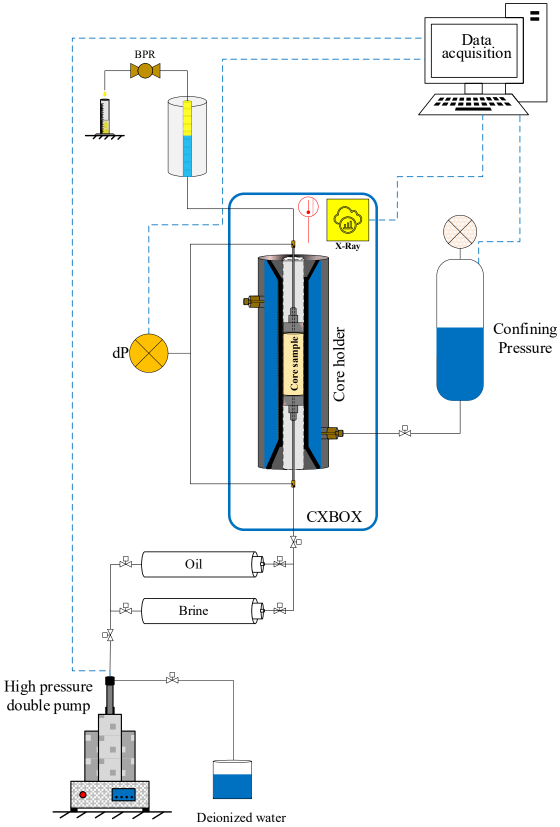

Fig. 2. Schematic representation of the WOWO experimental setup.

3 Results and discussion

3.1 Coreflood interpretation

Considering that all the coreflood steps were performed using the unsteady-state approach, it was possible to obtain water and oil relative permeability and capillary pressure curves for each step (from primary drainage to tertiary drainage).

As mentioned above, resident fluids production (water in case of drainage processes, oil in the case of imbibition), differential pressure between core inlet and outlet and longitudinal saturation profiles are the history-matched data to obtain K_r and P_c curves.

To illustrate the history-matching process and quality, we present in Fig. 3, Fig. 4 and Fig. 6 the example of sample KLT2-9 first imbibition history-matching. In Table 4, we present the flowrates used for this coreflood, as well as the capillary and Rapoport & Leas (RL) numbers.

Table 4. Flowrate, Capillary and Rapoport and Leas numbers during sample KLT2-9 first imbibition

Step	Q (cc/h)	Ca (dimensionless)	RL (cm²/min*cP)
1	6	6.0E-08	0.19
2	18	1.8E-07	0.56
3	36	3.6E-07	1.12
4	72	7.2E-07	2.23
5	150	1.5E-06	4.65

All corefloods interpretations presented in this paper have followed the same quality control check as the presented history match.

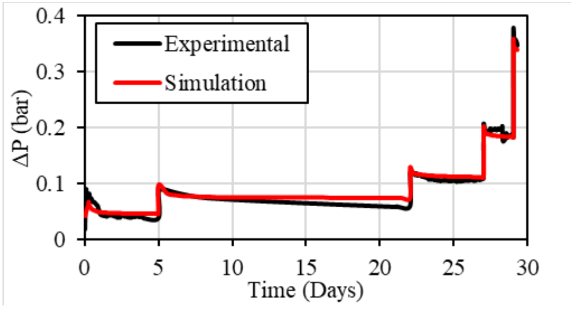

Fig. 3. Example of a differential pressure data history-match for a first imbibition process.

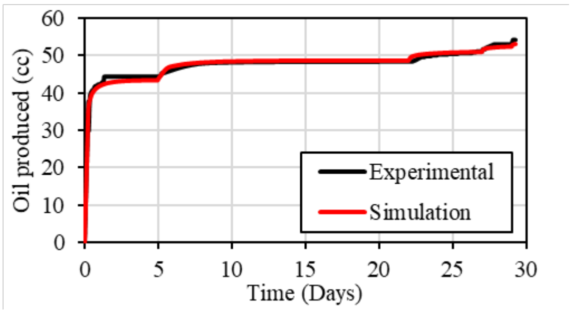

Fig. 4. Example of the oil production monitoring and the history-match for KLT2-9 first imbibition.

The acquired 2D saturation profiles are presented in Fig. 5. These profiles were then converted to 1D saturation profiles to perform the history match (on this step, additional profiles before water BT were added to improve the history match). In Fig. 6 we present the experimentally obtained saturation profiles in dotted lines and the simulated saturation profiles in solid lines.

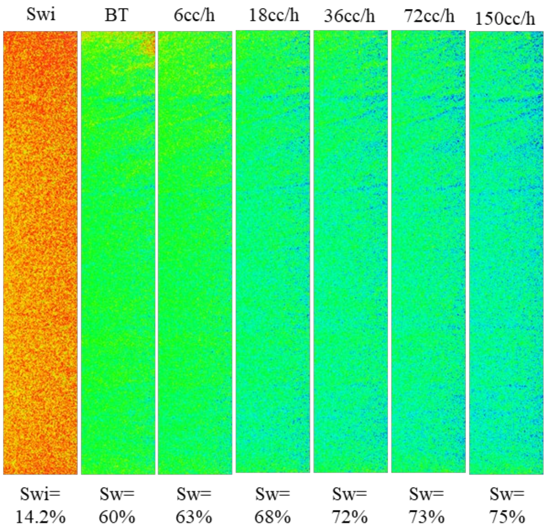

Fig. 5. 2D saturation profiles of KLT2-9 during first imbibition.

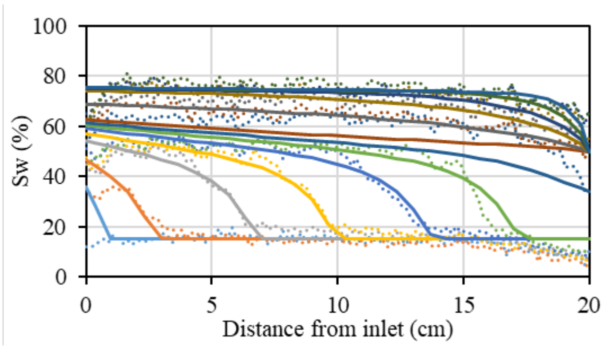

Fig. 6. Example of experimental 1D saturation profiles monitoring during KLT2-9 first imbibition (dotted lines) and simulated profiles after history-match (solid lines).

The history matches the pressure drops, the produced oil volume and 1D saturation profile monitoring during KLT2-9 waterflood provided first imbibition relative permeability and capillary pressure curves, are displayed in Fig. 7.

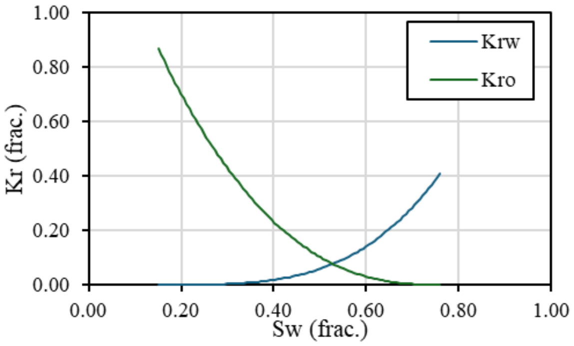

Fig. 7. Linear scale first imbibition relative permeability curves for sample KLT2-9.

It is important to state that the reference permeability value for relative permeability calculation is water permeability. This approach means that Krw(PD) starts at unity, where PD stands for primary drainage. Moreover, it is possible to notice on several results that $Kro_{,max}$ at the end of primary drainage is above unity. This behaviour has largely been discussed in the literature and is explained by a strongly water-wet system during primary drainage, where close to Swi water covers pore walls creating a less tortuous porous medium for the oil phase and generating a lubricating effect, thus increasing oil permeability at the low water saturation range (values close to Swi) [15].

In addition, the history-match allows the obtention of Pc *vs* Sw curves as well. To obtain reliable Pc curves for the complete range of Sw, it is important to constrain Pc interpretation with saturation profiles monitoring, especially for the saturation range prior to breakthrough (BT), interval beyond the unsteady-state range of validity. In addition, recent works showed the enhanced quality of matches that benefited from transient profiles calibration through history match [19]. Therefore, we have matched the saturation profiles prior BT to control the shape of the Pc(Sw) curve and obtained the Pc crossing point (Sw at Pc= 0) with the converging water saturation value at the core outlet. An example of capillary pressure curve obtained after history match and for which the quality control approach described was adopted is presented in Fig. 8. It corresponds to sample KLT2-9 first imbibition capillary pressure obtained during the history match described above.

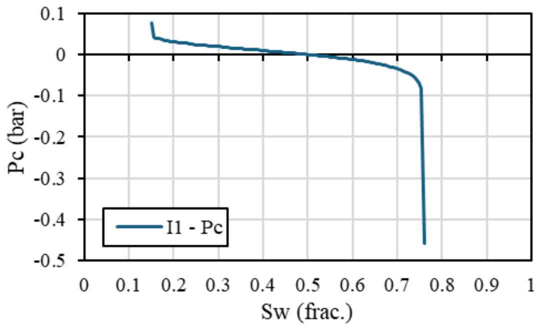

Fig. 8. KLT2-9 first imbibition capillary pressure curve.

The basic concept of Amott indexes rely on the relationship between spontaneous and forced displacements. Taking Fig. 9 as guide and considering parameters a, b, c, d and e, spontaneous displacements are defined as the variation of saturation between saturation at maximum Pc (positive Pc for imbibition and negative Pc for drainage) and saturation at Pc= 0 - *a* for spontaneous imbibition and *c* for spontaneous drainage. Forced displacements are defined as the variation of saturation between saturation at Pc= 0 and end-point saturation (negative Pc for forced imbibition, *b*, and positive Pc for forced drainage, *d*). Therefore, as we have Pc curves from the interpretation of all the corefloods and these Pc are constrained by the saturation profiles, we have confidence to derive a wettability index from these curves.

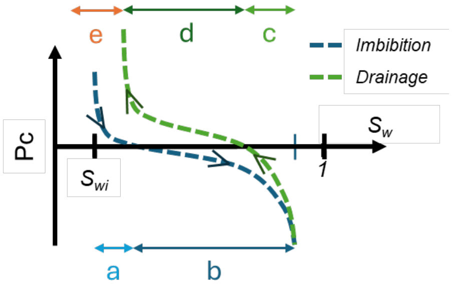

Fig. 9. Schematic representation of imbibition-drainage Pc sequence, with parameters indicating the spontaneous and forced steps.

The Amott* index was developed to consider the water trapped above Swi, that is called e in Fig. 9 presented above and is an indicative of non-water-wet behavior [20]. The deep fundamental understanding of the Amott* index is discussed in Bourgeois et al. (2024) [21], but the formulation is detailed in eq :(3), (4) and (5)

$$Amott^* = I_w - I_o^* \tag{3}$$

$$I_w = \frac{a}{a+b} \tag{4}$$

$$I_o^* = \frac{c+e}{c+d+e} \tag{5}$$

The calculation of this index is used in this work as a strategy to assess the wettability of the cores when no Amott-Harvey data is available.

It is important to highlight that the whole set of Kr curves presented in this work are a result of interpreted unsteady-state corefloods, that have a validity interval between injected fluid BT and remaining saturation at the end of the coreflood process. Therefore, the interval that falls beyond these bounds is an interpolation of the interpretation. Because of this limitation of unsteady-state corefloods interpretation, we chose to display the extrapolation of the Kr curves between remaining and residual fluids saturation with dots.

Another important point to be highlighted is the behavior of PD and I1 Kro close to Swi: primary drainage is performed by oil flood, which may induce a saturation gradient that remains even after bump rates. In this case, a part of the sample is at Swirr but the average core saturation is equal to Swi (Swi ≥ Swirr). This saturation gradient is then eliminated by performing oil flood reverse flow, that homogenizes the saturation profile at the average target Swi to eliminate the saturation gradient that could induce non-homogeneous wettability alteration. Meanwhile, in order to properly simulate fluids behavior during primary drainage, we need to extend Kr,PD until Swirr even though the experimental average saturation finishes at Swi. In addition, the imbibition process (Kr,I1) starts at Swi, as the core presents a homogeneous saturation profile at Swi after ageing.

In addition, during the ageing step, oil permeability at Swi may change, in a process usually related to wettability alteration and fluid distribution alteration at the pore scale. This change induces an instability between Kro,PD and Kro,I1 at Swi, that was observed in some of the results presented in the next sections.

3.2 WOWO experiments on SLT samples

It is important to state that the two W/O experimental cycles were performed on samples of different lithologies and sedimentary classification. This limits the possibility of correlating the results and comparing them directly. Moreover, using a different oil during waterflooding increases the difficulty on the results comparability, as the viscosity ratio between both W/O experiments are different ($\mu_o/\mu_w = 1.50$ for sample SLT2-10 imbibition and $\mu_o/\mu_w = 4.85$ for sample SLT1-10 imbibition).

Furthermore, it has been related that more oil-wet behavior during imbibition may be observed in experiments performed at room temperature [22], which is the case of sample SLT2-10 imbibition. This is most probably related to the higher viscosity ratios observed in these cases compared to experiments performed at higher temperature, such as in the case of SLT1-10, that was done at 90°C. On corefloods performed at room temperature, oil/water viscosity ratio and IFT are higher than oil/water viscosity ratio and IFT at high temperature. This may lead to more unstable coreflood at lower temperature than at higher temperature, inducing earlier breakthrough and more pronounced diphasic production, parameters associated to oil-wettability.

When we plot both imbibition interpreted relative permeabilities together, as presented in Fig. 10, it is clearly visible that the experiment performed at 90 °C with a less favorable viscosity ratio to water has larger oil trapping as its residual oil saturation is higher. Moreover, this is complemented by a higher water relative permeability overall, whereas imbibition oil relative permeabilities have roughly the same shape.

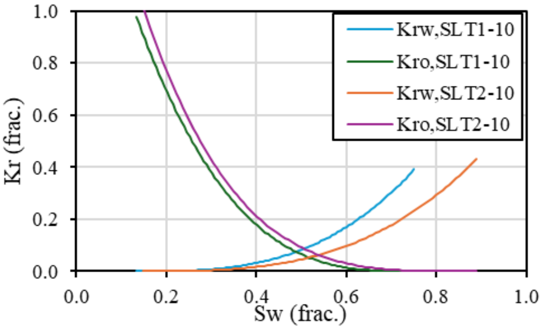

Fig. 10. Samples SLT1-10 and SLT2-10 imbibition relative permeability curves.

3.1.1 SLT1-10

Regarding sample SLT1-10 behaviour during the coreflooding cycles, we observed negative hysteresis in Kro, with oil relative permeability reduction, and positive hysteresis in Krw curves, with increasing water relative permeability, between primary drainage and imbibition 1. In addition, Kro and Krw experimented both further mobility reduction during Drainage 2 and stabilization for subsequent cycles (I2-D3). It is important to state that Krw > Krw(PD) for all the coreflooding cycles. The curves used for this analysis are presented in Fig. 11 and Fig. 12. The arrows in the curves indicate the saturation change direction of the coreflood, the color gradient represents the step change, red colored lines always represent primary drainage Krw and Kro and the dotted line is the extension from the remaining fluid saturation (experimental) until residual fluid saturation (obtained after interpretation).

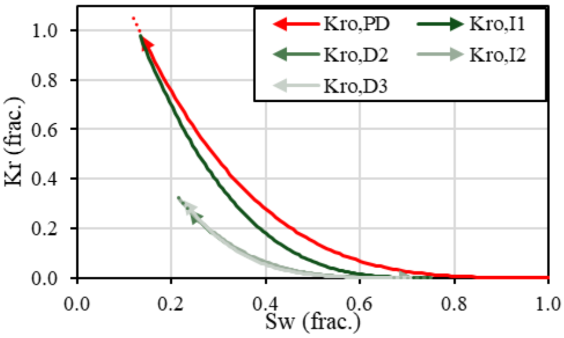

Fig. 11. Kro curves obtained for the sequence PD-I1-D2-I2-D3 for sample SLT1-10.

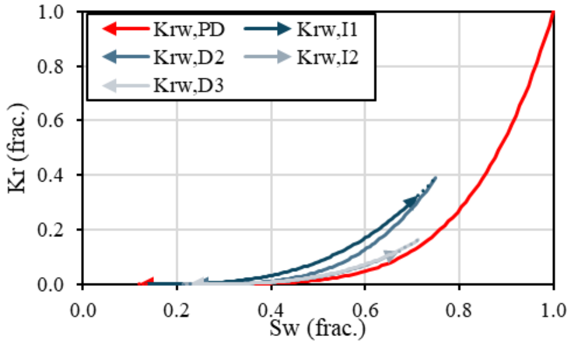

Fig. 12. Krw curves obtained for the sequence PD-I1-D2-I2-D3 for sample SLT1-10.

In addition, from the set of relative permeability curves, we calculated the Amott* for the two drainage-imbibition cycles, that indicate a water-wet core. The results are presented in Table 5.

Table 5. SLT1-10 Amott* wettability indexes for I1-D2 and I2-D3 cycles

$I_{W}1$	$I_{O}^{*}1$	$I_{A}^{*}1$
0.547	0.107	**0.440**
$I_{W}2$	$I_{O}^{*}2$	$I_{A}^{*}2$
0.037	-0.117	**0.154**

3.1.2 SLT2-10

When evaluating the hysteresis of the corefloodin g cycles of sample SLT2-10, it is possible to see that both fluids mobility are reduced from imbibition 1 to drainage 2, as presented in Fig. 13 and Fig. 14.

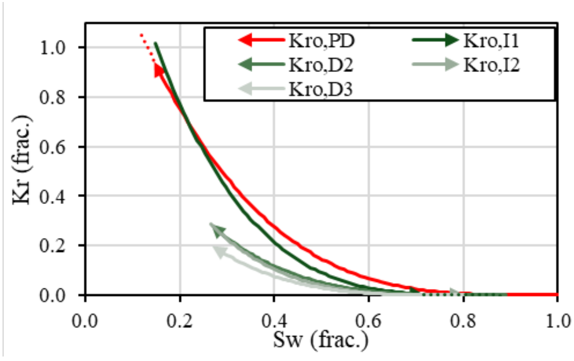

Fig. 13. Kro curves obtained for the sequence PD-I1-D2-I2-D3 for sample SLT2-10.

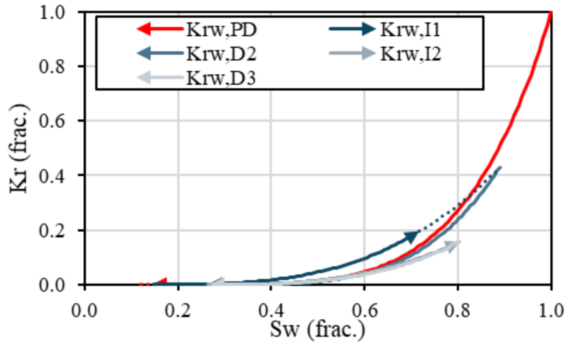

Fig. 14. Krw curves obtained for the sequence PD-I1-D2-I2-D3 for sample SLT2-10.

Nonetheless, when analyzing the subsequent coreflood steps (D2-I2-D3), we have different behaviors for Krw and Kro. Water mobility is reduced from D2 to I2 and then no more hysteresis is observed. On the other hand, oil mobility stays the same from D2 to I2 but reduces from I2 to D3.

One interesting point to observe is the fact that none of the experiments was able to retrieve the same level of Swi obtained at the end of Primary Drainage. This behaviour is usually related to mixed-wet samples and is quite known in the literature [20], [23]**.** Even though departing from a higher initial water saturation than Swirr, no further recovery is expected as oil trapping increases after each imbibition process.

This cycle-dependent behaviour is not what is modelled by classical hysteresis models, but such results have already been related by some authors, such as [24] and [25], that have worked both on preserved, mixed-wet, reservoir and Berea cores. They have observed a significant hysteresis in Krow between secondary drainage and first imbibition (Krow (Drainage 2) < Krow (Imbibition 1)) and also a hysteresis in Krwo between the same steps (Krw (Drainage 2) < Krw (Imbibition 1)). The hysteresis in the Krw between cycle is greater than in the Krow. This indicates that, large number of pores were oil-wet.

Nevertheless, it is clear that no further oil recovery is expected even after starting imbibition cycles at higher values of Swi, as more fluid is trapped after performing the different coreflooding cycles.

The computed Amott* indexes are presented in Table 6 and represent a neutral to slightly oil-wet system.

Table 6. SLT2-10 Amott* wettability indexes for I1-D2 and I2-D3 cycles

$I_{W}1$	$I_{O}^{*}1$	$I_{A}^{*}1$
0.223	0.289	**-0.066**
$I_{W}2$	$I_{O}^{*}2$	$I_{A}^{*}2$
0.000	0.193	**-0.193**

3.2 KLT experiments

3.2.1 KLT2-8

The core identified as KLT2-8 has a sedimentary classification of 8 and belongs to a different reservoir level than the cores identified as KLT3. A notable difference is observed in poro-perm values between this core and the other ones, as it presents a high value of effective porosity. Nonetheless, the same experimental conditions and protocol were respected for initial states restoration and cyclic coreflood, which validates data and allows an evaluation regarding hysteresis models.

The obtained Kro and Krw curves between primary drainage and tertiary drainage are presented in Fig. 15 and Fig. 16, using the same graphical logic as the one used for the presentation of SPS-1 samples results.

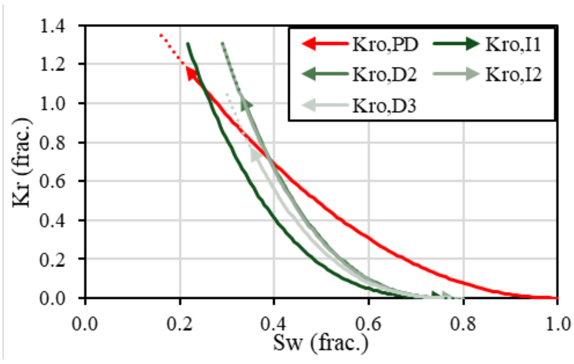

Fig. 15. Kro curves obtained for the sequence PD-I1-D2-I2-D3 for sample KLT2-8.

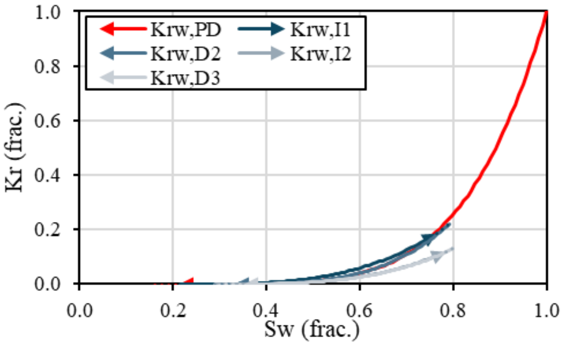

Fig. 16. Krw curves obtained for the sequence PD-I1-D2-I2-D3 for sample KLT2-8.

The Krw of the first imbibition and secondary drainage superimpose the Krw of the primary drainage which is not representing a bounding curve as initially claimed in the Killough model.

Regarding Kro, primary drainage oil relative permeability does not act as bounding curve of the subsequent cycles, as each curve move towards and cross the primary drainage Kro, counterpart as stated by the Beattie et al. model [7] and yet verified by [12], [26].

The result of the Amott* analysis is presented in Table 7 and indicates a water-wet core.

Table 7. KLT2-8 Amott* wettability indexes for I1-D2 and I2-D3 cycles

Iw1	Io*1	I_A*1
0.770	0.338	**0.432**
Iw2	**Io*2**	**I_A*2**
0.653	0.558	**0.096**

3.2.2 KLT1-8

Core KTL1-8 has a sedimentary classification of 8 like KLT2-8 but is originated from another reservoir level. Although belonging to the same sedimentary classification, it does not have the same poro-perm properties as KLT2-8.

When analyzing the behavior of both phases Krs, it is possible to observe that the trend of the Kro and Krw curves through the cycle is better defined related to the boundary curves (primary drainage Krw and Kro). Oil mobility decreases from imbibition 1 and is lower than oil mobility during primary drainage during the whole cycle. On the other hand, water mobility increases from primary drainage to imbibition 1 and remains higher than primary drainage Krw for the totality of the coreflood cycles. These observations are presented in Fig.17 and Fig. 18. Again, the Kro drainage and imbibition cycles move towards the bounding primary drainage curve, but not as scanning curves as stated by Killough's model.

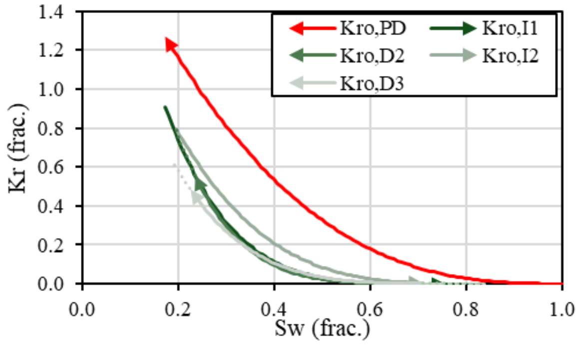

Fig.17. Kro curves obtained for the sequence PD-I1-D2-I2-D3 for sample KLT1-8.

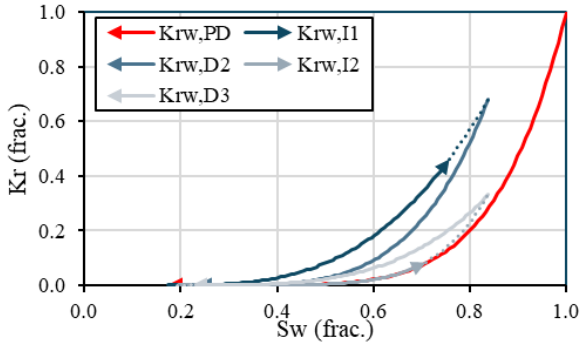

Fig. 18. Krw curves obtained for the sequence PD-I1-D2-I2-D3 for sample KLT1-8.

In terms of wettability, the computed Amott* in the I1-D2 and I2-D3 cycles are presented in Table 8. These values are representative of neutral to slightly oil wet systems. The end-points Krs and saturations reflect the same wettability interpretation, following the definition of the rule of thumb [23], [27].

Table 8. KLT1-8 Amott* wettability indexes for I1-D2 and I2-D3 cycles

Iw1	Io*1	I_A*1
0.303	0.582	**-0.279**
Iw2	**Io*2**	**I_A*2**
0.241	0.593	**-0.352**

Very small amount of water was trapped along the cycles and residual oil after the imbibition processes was constant. This denotes constant recovery despite the loss in mobility.

3.2.3 KLT2-9

Core KLT2-9 is the only one in this study that belongs to a sedimentary classification 9. During the experimental cycle of KLT2-9, drainage 3 was not possible to be carried out due to operational issues. Therefore, the cyclic coreflooding ends at the end of imbibition 2.

Regarding oil relative permeability, this is the only case in the whole study where an LET model [28] was used for the history-match of primary drainage. This approach is usually adopted in the case of non-monomodal distribution of porosities. In the case of this core, as no twin plug MICP was available, a T2 relaxation time distribution measurement was taken to assess the rock pore size distribution. This measurement is systematically performed on brine-saturated twin plugs taken at close depths, from the same sedimentary classification and equivalent poro-perm values (as in the case of MICP runs). The T2 relaxation time distribution confirms the multi-modal porosity distribution of the plug, validating the LET approach for primary drainage. In addition, measured values of Kro at the equilibrated flow rates during primary drainage indicated an s-shaped Kro form. The result of the T2 relaxation time distribution is presented in Fig. 19.

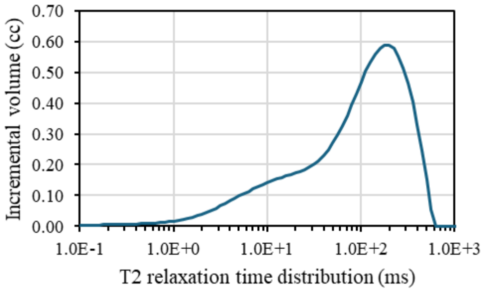

Fig. 19. T2 relaxation time distribution performed on a brine-saturated twin-plug of KLT2-9.

Regarding mobility analysis, a reduction in mobility from primary drainage Kro that remains for the subsequent steps of the cyclic corefloods is observed. In addition, it is possible to observe that D2 and I2 Kro follow the same path, indicating no further Kro hysteresis from D2 on. Such behavior was not noticed in any of the other coreflooding cycles. These results are presented in Fig. 20.

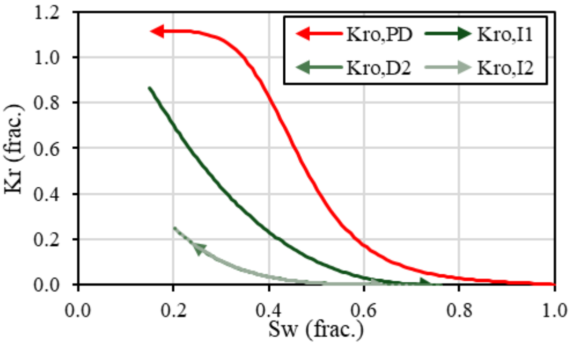

Fig. 20. Kro curves obtained for the sequence PD-I1-D2-I2-D3 for sample KLT2-9.

In terms of water relative permeability hysteresis, an increase of water mobility compared to primary drainage was observed during I1. Moreover, an interesting behaviour regarding Krw mobility evolution was observed: D2-Krw followed the same path as its precedent coreflood (I1-Krw), but I2 indicated a consequent mobility reduction and higher Sor, with I2-Krw@Sor lower than Krw bounding curve. These results are presented in Fig. 21.

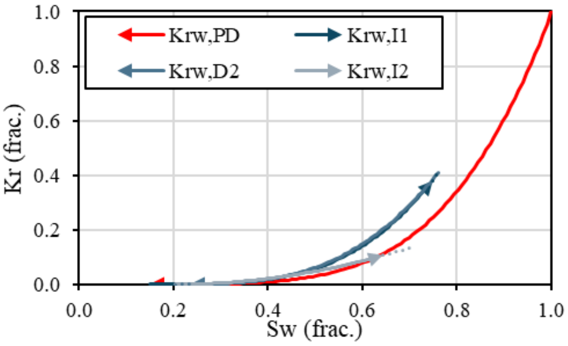

Fig. 21. Krw curves obtained for the sequence PD-I1-D2-I2-D3 for sample KLT2-9.

The result of the Amott* analysis of core KLT2-9 is presented in Table 9 and indicates a slightly water-wet core.

Table 9. KLT2-9 Amott* wettability indexes for I1-D2 cycle

I_W1	I_O*1	I_A*1
0.585	0.306	**0.279**

3.2.4 KLT3-10

Core KLT3-10 belongs to the same sedimentary classification as SLT2-10, but as they come from different fields, they have completely different poro-perm properties.

Kro analysis through the cyclic corefloods indicates mobility reduction of all the cycles from I1 to D3 compared to primary drainage Kro bounding curve. Moreover, for cycles D2 and D3, reaching the same Swi level obtained at the end of primary drainage was not possible, with considerably higher values of RWS2 and RWS3 (remaining water saturation after drainage 2 and 3, respectively). The same observation is done for core SLT2-10 (same sedimentary classification). The group of Kro curves for KLT3-10 cyclic coreflood is presented in Fig. 22.

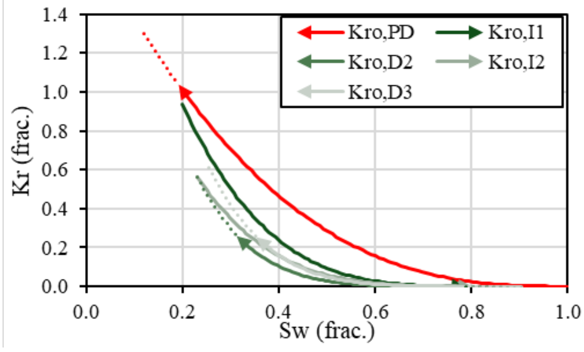

Fig. 22. Kro curves obtained for the sequence PD-I1-D2-I2-D3 for sample KLT3-10.

Regarding Krw curves, it is possible to observe mobility reduction through the cycles, with Krw < Krw(PD) for all the cyclic Kr curves. Similar to what is stated for Kro, Krw mobility reduction was also observed in the case of sample SLT2-10. Such behavior for Krw and Kro curves is not dealt by Killough's model, with both phases' mobility reduction through the cycles. The group of Krw curves for KLT3-10 coreflooding cycles is presented in Fig. 23.

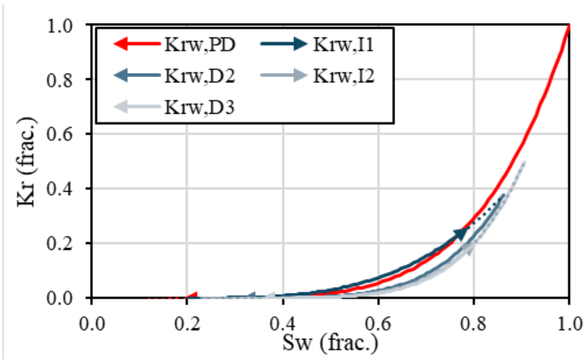

Fig. 23. Krw curves obtained for the sequence PD-I1-D2-I2-D3 for sample KLT3-10.

The computed Amott* indexes for core KLT3-10 are presented in Table 10 and represent a neutral to slightly water-wet system.

Table 10. KLT3-10 Amott* wettability indexes for I1-D2 and I2-D3 cycles

I_{W1}	I_O*1	I_A*1
0.428	0.255	**0.173**
I_{W2}	**I_O*2**	**I_A*2**
0.143	0.290	**-0.147**

3.3 Discussion

The first objective of this paper is to check whether it is possible to model the different corefloods with Killough's model, as it is the only model accounting for both phases' hysteresis implemented on most commercial simulators. It is interesting to observe that all the cyclic, unsteady-state corefloods interpreted have, at least, one coreflood cycle that crosses the boundary K_r curves, indicating the non-possibility to model the hysteresis effects with the Killough model. This situation may be explained by the fact that primary drainage relative permeability curves that define the bounding curves are obtained under a different wettability condition than the subsequent coreflood Kr curves, as ageing in crude oil is performed between primary drainage and first imbibition.

It is important to notice that Killough's model assumes that imbibition relative permeability curves are reversible, and it considers Land's trapping model. These hypotheses make it non-applicable on the experimental data presented in the paper, as we have cases departing from water-wetness.

Regarding Krw, most of the curves between primary drainage and first imbibition follow a trend that respects the Killough model, as Krw (I1) > Krw (PD).

Drainage 2 Krw curves follow trends that may be related to the core's wettability: cores presenting stronger water-wettability have Drainage 2 Krw following the same path as Imbibition 1 Krw, indicating no to very little hysteresis on the wetting phase. This is the case of cores SLT1-10, KLT2-8 and KLT2-9. On the other hand, for cores presenting less preference to water (neutral to slightly water-wet), a larger hysteresis is observed, with systematic water mobility reduction. The subsequent cycles (Imbibition 2 and Drainage 3) present an interesting behavior, with water mobility reduction between D2 and I2 and no more hysteresis between I2 and D3 (the only case where this behaviour is not observed is for core KLT1-8). This difference in behaviour of KLT1-8 compared to the others may be explained by a difference in wettability, that was observed in both Amott*1 and Amott*2 results. As a reminder, core KLT1-8 has the same sedimentary classification as core KLT2-8 but comes from a different reservoir level, thus aged with dead oil of different composition. A compilation of these results is presented in Fig. 24.

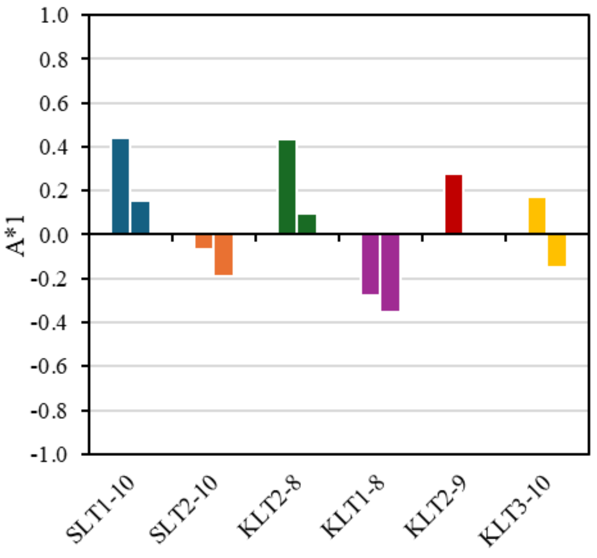

Fig. 24. Compilation of Amott*1 and Amott*2 results for the cores analyzed in this paper.

The same analysis indicates an even more pronounced effect of the mobility reduction through cycles on Kro curves, that are systematically lower than the primary drainage Kro bounding curve from the very first imbibition. Kro values lower than Kro(PD) is what is implemented on Killough's model. However, the main incompatibility is that, on Killough's model, cyclic corefloods oil mobility at critical saturation meets Kro bounding curve. Critical fluid saturation refers to the minimum fluid saturation below which the phase becomes immobile. This behaviour was not seen on any of the cyclic corefloods, except for sample KLT2-8. Cycle-dependent oil mobility reduction was systematically observed.

Furthermore, interesting results regarding residual saturations were observed, as higher water trapping during Drainage 2 does not necessarily mean higher oil recovery during Imbibition 2. This situation is clearly seen in the case of cores SLT1-10, SLT2-10, KLT2-8, KLT1-8 and KLT2-9. Interestingly, KLT3-10 core indicates a higher oil recovery during Imbibition 2 departing from RWS2>Swi.

4 Conclusion

In this study, six cyclic water/oil (WOWO) unsteady-state relative permeability results were presented. The hysteresis was interpreted in terms of system wettability, phase mobility and saturation history. The results of this study demonstrated that the Killough model is not able to predict the hysteretic behavior of mixed-wet system. The results showed that hysteresis is present in both oil and water relative permeability. Kr hysteresis is associated with mobility reduction in a cycle-dependent way (in most of the tested cores). Such reduction contrasts with the subsequent scanning curves implemented in the reservoir simulator based on the Killough model. The different observations made in the results presented in this study and the integration of diverse characteristics (sedimentary classification, poro-perm and wettability) will enable us to build a better-suited hysteresis model for mixed-wet reservoirs.

An important way forward on this topic is to extend the new proposed model to integrate Pc hysteresis as well, in order to capture and represent experimental observations on mixed-wet turbidites.

References

[1] V. Joekar-Niasar, F. Doster, R. T. Armstrong, D. Wildenschild, and M. A. Celia, "Trapping and hysteresis in two-phase flow in porous media: A pore-network study," *Water Resour. Res.*, vol. 49, no. 7, pp. 4244–4256, 2013, doi: 10.1002/wrcr.20313.

[2] G. Li and J. Yao, "Snap-off during imbibition in porous media: Mechanisms, influencing factors, and impacts," *Eng*, vol. 4, no. 4, pp. 2896–2925, 2023.

[3] A. Rezaei, H. Abdollahi, Z. Derikvand, A. Hemmati-Sarapardeh, A. Mosavi, and N. Nabipour, "Insights into the effects of pore size distribution on the flowing behavior of carbonate rocks: Linking a nano-based enhanced oil recovery method to rock typing," *Nanomaterials*, vol. 10, no. 5, pp. 1–22, 2020, doi: 10.3390/nano10050972.

[4] X. Zhou, N. R. Morrow, and S. Ma, "Interrelationship of wettability, initial water saturation, aging time, and oil recovery by spontaneous imbibition and waterflooding," *Spe J.*, vol. 5, no. 2, pp. 199–207, 2000.

[5] P. P. Jadhunandan and N. R. Morrow, "Effect of wettability on waterflood recovery for crude-oil/brine/rock systems," *SPE Reserv. Eng.*, vol. 10, no. 1, pp. 40–46, 1995.

[6] J. E. Killough, "Reservoir simulation with history-dependent saturation functions," *Soc. Pet. Eng. J.*, vol. 16, no. 1, pp. 37–48, 1976.

[7] C. I. Beattie, T. C. Boberg, and G. S. McNab, "Reservoir simulation of cyclic steam stimulation in the Cold Lake oil sands," in *SPE Western Regional Meeting*, 1989, p. SPE-18752.

[8] A. Kjosavik, J. K. Ringen, and S. M. Skjaeveland, "Relative permeability correlation for mixed-wet reservoirs," in *SPE Improved Oil Recovery Conference?*, 2000, p. SPE-59314.

[9] E. J. Spiteri, R. Juanes, M. J. Blunt, and F. M. Orr, "A new model of trapping and relative permeability hysteresis for all wettability characteristics," *SPE J.*, vol. 13, no. 3, pp. 277–288, 2008, doi: 10.2118/96448-PA.

[10] S. M. Skjaeveland, L. M. Siqveland, A. Kjosavik, W. L. Thomas, and G. A. Virnovsky, "Capillary pressure correlation for mixed-wet reservoirs," *SPE Reserv. Eval. Eng.*, vol. 3, no. 1, pp. 60–67, 2000.

[11] P. Egermann, O. Vizika, L. Dallet, C. Requin, and F. Sonier, "Hysteresis in three-phase flow: experiments, modeling and reservoir simulations," in *SPE Europec featured at EAGE Conference and Exhibition?*, 2000, p. SPE-65127.

[12] S. Foroudi, A. Gharavi, and M. Fatemi, "Assessment of two-phase relative permeability hysteresis models for oil/water, gas/water and gas/oil systems in mixed-wet porous media," *Fuel*, vol. 309, p. 122150, 2022.

[13] G. Puyou, M. N'Guyen, and S. Savin, "CXBOX: An Innovative Tool For Fluid Dynamic Quantification During Corefloods," in *Proc. SCA International Symposium*, 2017.

[14] A. Graue, E. Aspenes, T. Bognø, R. W. Moe, and J. Ramsdal, "Alteration of wettability and wettability heterogeneity," *J. Pet. Sci. Eng.*, vol. 33, no. 1–3, pp. 3–17, 2002.

[15] C. McPhee, J. Reed, and I. Zubizarreta, *Core analysis: a best practice guide*. Elsevier, 2015.

[16] M. J. Blunt, *Multiphase flow in permeable media: A pore-scale perspective*. Cambridge university press, 2017.

[17] "CYDAR – User Manual Dispersion module CYDAR – USER MANUAL Dispersion module".

[18] R. Lenormand, K. Lorentzen, J. G. Maas, and D. Ruth, "Comparison of four numerical simulators for SCAL experiments," *Petrophysics*, vol. 58, no. 1, pp. 48–56, 2017.

[19] S. Berg, H. Dijk, E. Unsal, R. Hofmann, B. Zhao, and V. R. Ahuja, "Simultaneous determination of relative permeability and capillary pressure from an unsteady-state core flooding experiment?," *Comput. Geotech.*, vol. 168, p. 106091, 2024.

[20] S. K. Masalmeh, "Experimental measurements of capillary pressure and relative permeability hysteresis," in *Paper SCA 2001-23 presented at the SCA Conference, Edinburgh, Scotland, September*, 2001.

[21] M. Bourgeois, B. Satken, P. Goyal, S. S. Al Eissaee, C. Cottin, and E. Draoui, "Using WAG Laboratory Data to Derisk Water Injection at the Gas-Oil Contact on a Giant Offshore Field," in *Abu Dhabi International Petroleum Exhibition and Conference*, 2024, p. D011S009R002.

[22] M. Sarmadivaleh, A. Z. Al-Yaseri, and S. Iglauer, "Influence of temperature and pressure on quartz–water–CO2 contact angle and CO2–water interfacial tension," *J. Colloid Interface Sci.*, vol. 441, pp. 59–64, 2015.

[23] S. K. Masalmeh, "The effect of wettability on saturation functions and impact on carbonate reservoirs in the middle east," in *Abu Dhabi International Petroleum Exhibition and Conference*, 2002, p. SPE-78515.

[24] F. H. L. Wang, "Effect of wettability alteration on water/oil relative permeability, dispersion, and flowable saturation in porous media," *SPE Reserv. Eng.*, vol. 3, no. 2, pp. 617–628, 1988.

[25] E. M. Braun and R. F. Holland, "Relative permeability hysteresis: laboratory measurements and a conceptual model," *SPE Reserv. Eng.*, vol. 10, no. 3, pp. 222–228, 1995.

[26] M. Fatemi and M. Sohrabi, "Mechanistic study of enhanced oil recovery by gas, WAG and SWAG injections in mixed-wet rocks: Effect of gas/oil IFT," *Exp. Therm. Fluid Sci.*, vol. 98, pp. 454–471, 2018.

[27] A. Mirzaei-Paiaman, "New methods for qualitative and quantitative determination of wettability from relative permeability curves: Revisiting Craig's rules of thumb and introducing Lak wettability index," *Fuel*, vol. 288, p. 119623, 2021.

[28] F. Lomeland, E. Ebeltoft, and W. H. Thomas, "A new versatile relative permeability correlation," in *International symposium of the society of core analysts, Toronto, Canada*, 2005, vol. 112.

APPENDIX

Table 11. Cores grain size and sorting

Cores	Grain size	Grain sorting
SLT1-10	Medium to granule	Very poorly sorted
SLT2-10	Medium to very coarse	Poorly sorted
KLT2-8	Fine to medium	Well sorted
KLT1-8	Fine grained to granule	Poorly sorted
KLT2-9	Fine to medium grained	Well sorted
KLT3-10	Fine grained to pebble	Poorly sorted

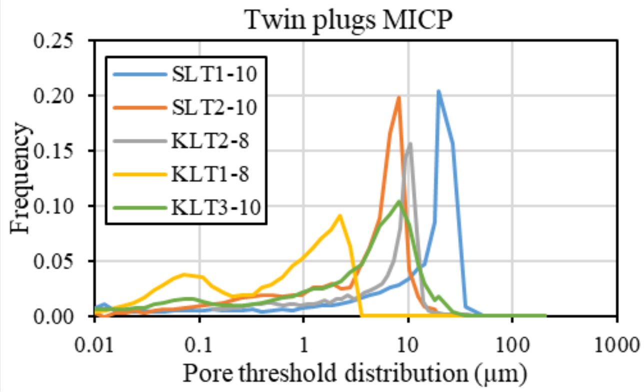

Fig. 25. Twin plugs MICP measurements.

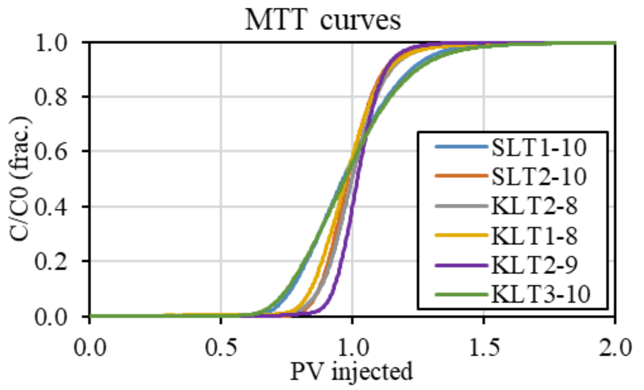

Fig. 26. Miscible tracer tests used to attest cores longitudinal homogeneity and suitability to undergo unsteady-state corefloods.

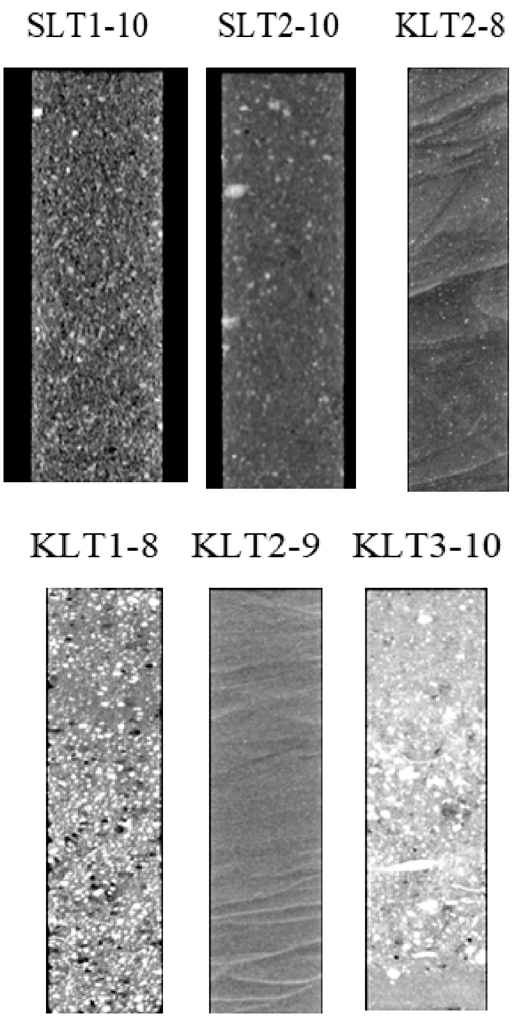

Fig. 27. CT scans of cores from the SLT and KLT series. Top row: SLT1-10, SLT2-10, KLT2-8. Bottom row: KLT1-8, KLT2-9, and KLT3-10.